ISSN:1738-6764, eISSN:2093-7504

A Study on the Parametric Design and Performance Optimization of Hubless Rim-Driven Thruster for Small-Scale Marine Vehicles

Zhiwen Liu [1] and Myeon-Gyun Cho [2,*]

[1] Ph.D. Student, Semyung University; liuzhiwen504@gmail.com
[2] Professor, Semyung University; mg_cho@semyung.ac.kr
* Correspondence

https://doi.org/10.5392/IJoC.2026.22.1.096

Manuscript Received 2 December 2025; Received 5 January 2026; Accepted 19 January 2026

Abstract: *The growing demand for efficient and reliable propulsion systems in small and medium-sized vessels has revealed the limitations of conventional shaft-based systems, which often suffer from low transmission efficiency, high maintenance costs, and excessive noise and vibration. Even advanced pod-type propulsors frequently fail to meet the specific efficiency needs of small underwater vehicles operating in confined spaces. The hubless rim-driven thruster (RDT) presents a novel propulsion concept by integrating the ducted propeller and electric motor into a single, compact unit, eliminating the traditional bulky shaft and sealing components. This design enhances hydrodynamic efficiency and offers superior resistance to entanglement, making it an ideal solution for challenging marine environments. This study explores the parametric design and optimization of hubless RDT blades to enhance propulsive performance in shallow-water and small-scale underwater applications. Using STAR-CCM+ simulations, we systematically analyze the impact of paddle blade pitch angle and chord length on hydrodynamic performance. The resulting comprehensive dataset is utilized to train a machine learning surrogate model, facilitating rapid performance prediction and optimization. By employing an improved adaptive Sparrow Search Algorithm, we identify the optimal geometric parameters, achieving a 3–7% increase in propulsion efficiency while maintaining structural reliability under optimal operating conditions. The findings of this research provide a robust, data-driven methodology for designing the next generation of highly efficient and reliable propulsion systems for small underwater vehicles, contributing significantly to the field of marine engineering.*

Keywords: Rim-driven Thruster; Propulsive Efficiency; Computational Fluid Dynamics (CFD); Machine Learning

1. Introduction

With the rapid growth of international maritime trade, the demand for efficient shipping logistics has increased significantly, driving the enlargement of vessel sizes and creating new requirements for propulsion systems. Conventional shaft-driven propellers occupy substantial space, incur high maintenance costs, and suffer from low transmission efficiency and energy losses. Moreover, their operation generates noise and vibration, which compromise vessel stability and stealth [1]. Podded propulsion systems offer certain improvements but still fail to meet the efficiency and maneuverability demands of modern ships.

The Rim-driven thruster (RDT) has emerged as a promising alternative by integrating a ducted propeller and an electric motor into a compact rim structure [2-4]. This configuration eliminates the traditional shaft and hub system, reducing mechanical losses, noise, and vibration. Early RDT designs retained a central hub to improve structural strength; however, the hub obstructed flow and increased the risk of entanglement with aquatic debris. Hubless RDT overcome these limitations, offering improved hydrodynamic efficiency, enhanced anti-fouling capability, and superior stealth characteristics, which make them particularly attractive for underwater vehicles, unmanned surface vehicles (USVs), and military platforms [5, 6].

In recent years, small and medium-sized vessels—including tugboats, USVs, and underwater robots—have received increasing attention due to their adaptability in shallow waters and confined environments [7-9]. However, conventional propellers face several inherent drawbacks in such applications: exposed blades are prone to debris entanglement [10], maneuverability is limited by rudder-based control systems [11], and cavitation at high rotational speeds leads to efficiency degradation, structural erosion, and excessive noise [12]. In contrast, RDT can provide efficiency improvements of approximately 10–20% compared with traditional propellers, while simultaneously enhancing maneuverability and operational reliability [13, 14].

Since the concept of the rim-driven thruster was first introduced by Kort in 1940 [15], advances in electric motor technology and composite materials have significantly improved RDT feasibility and performance. RDT technology has been identified as strategically important for future submarine and underwater vehicle development [16], and several successful prototypes and commercial products have been reported, demonstrating long-term operational stability and growing industrial maturity [17-20]. These developments highlight the strong potential of hubless RDTs as next-generation propulsion devices for intelligent marine platforms.

Current research on RDT hydrodynamics primarily relies on experimental testing and numerical simulation. Due to the high cost and complexity of experimental studies, computational fluid dynamics (CFD) has become the dominant research tool [21, 22]. Existing studies have investigated the effects of blade number, duct geometry, and key design parameters on RDT performance [23-27], as well as duct modifications [28], blade thickness distributions [29], and parametric design methods [30]. More recently, surrogate models and optimization algorithms, including neural networks combined with NSGA-II [31] as well as response surface methods [32], have been introduced to improve design efficiency. Nevertheless, most prior work focuses on conventional RDT configurations, while systematic parametric optimization of hubless blade designs remains limited. In addition, the integration of machine learning with advanced metaheuristic optimization algorithms for efficient and reliable hubless RDT design has received relatively little attention.

To address these gaps, this study proposes an integrated, data-driven framework for the parametric design and optimization of hubless rim-driven thrusters. The proposed methodology combines high-fidelity CFD simulations for data generation, a machine learning surrogate model for rapid performance prediction, and an Improved Adaptive Sparrow Search Algorithm (IASSA) for efficient optimization. By applying this framework to the systematic optimization of hubless RDT blade parameters, a CFD-verified propulsion efficiency improvement of 3–7% is achieved while maintaining structural feasibility. This study provides a reproducible and practical design methodology that bridges the gap between theoretical optimization and engineering application for small and medium-sized marine propulsion systems.

The structure of this paper is as follows: Section 2 details the RDT modeling methodology, including a new inverse thickness design approach, 3D modeling principles, blade coordinate transformations, and the underlying CFD theory. Section 3 outlines the blade optimization strategy, focusing on building surrogate models based on simulation data and introducing the IASSA for hyperparameter optimization. In this section, we define the input variables (blade area ratio, pitch ratio, and advance coefficient) and outputs (thrust and torque) to construct the surrogate models, with the objective of maximizing propulsion efficiency. Section 4 presents the results and analysis, where we compare the accuracy and efficiency of different models. We show how the IASSA-SVR model accurately maps the relationship between blade parameters and propulsion efficiency, leading to the identification of optimal parameter combinations. Finally, Section 5 provides a summary of the study, emphasizing the significance of our findings and discussing future development trends and application prospects for RDT.

2. Theoretical Background

This chapter details the foundational components and theoretical constructs employed in this study. It establishes the baseline geometry of the RDT, the mathematical framework for its parametric representation, and the computational instruments selected for surrogate modeling and optimization. These theoretical foundations provide essential support for the subsequent modeling, simulation analysis, and optimization design.

2.1 Overview of Hubless RDT Structure

The RDT is an advanced propulsion system that integrates the ducted propeller and the electric motor into a single compact ring (rim). Unlike traditional systems, the RDT eliminates the central shaft and gearbox, with the propeller blades being driven directly by the rim, which houses the motor's rotor. This design fundamentally improves hydrodynamic efficiency, reduces noise and vibration, and minimizes the risk of entanglement, making it highly suitable for applications in small underwater vehicles. Figure 1 illustrates the 3D model and key components of the hubless rim-driven thruster.

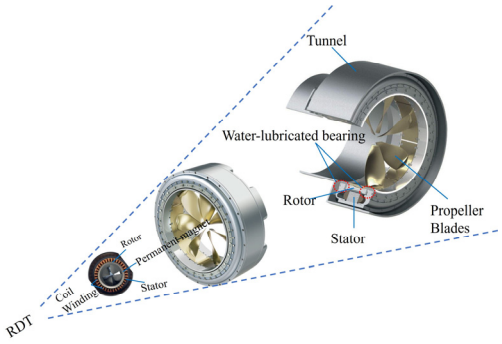

Figure 1. 3D Model and Key Components of the Hubless Rim-Driven Thruster

2.2 Hydrodynamic performance evaluation index

In the design and optimization process of a thruster, accurately evaluating its hydrodynamic performance is a fundamental and critical step. To quantitatively assess the propulsion efficiency and operating characteristics of RDT, several typical non-dimensional hydrodynamic performance coefficients are commonly employed, including the following [6]:

(1) Advance Coefficient (J)

The advance coefficient is used to characterize the ratio between the propeller's forward speed and its rotational speed, and is defined as:

$$J = \frac{V_A}{nD} \tag{1}$$

In the formula: V_A is the inlet velocity in m/s; n is the propeller rotating speed in r/min; D is the diameter.

(2) Thrust Coefficient (K_T)

The thrust coefficient is used to quantify the axial thrust generated by the propeller under unit inflow velocity conditions, and is defined as follows:

$$K_T = \frac{T}{\rho n^2 D^4} = \frac{T_N + T_P}{\rho n^2 D^4} \tag{2}$$

In the formula: ρ is the density of water; T is the overall thrust, T_N is the blade thrust, T_P is the duct thrust.

(3) Torque Coefficient (K_Q)

The torque coefficient reflects the propeller's ability to generate torque and is defined as:

$$K_Q = \frac{Q}{\rho n^2 D^5} \tag{3}$$

In the formula: Q is the propeller torque.

(4) Propulsive Efficiency (η)

Propulsive efficiency is a key indicator of the hydrodynamic performance of a propeller, representing its ability to convert input power into useful thrust power. It is expressed as:

$$\eta = \frac{K_T}{K_Q}\frac{J}{2\pi} \tag{4}$$

2.3 A brief introduction to approximate models and machine learning methods

2.3.1 BP neural network and RBF neural network

Backpropagation neural network is a type of multilayer feedforward neural network. It receives input signals through the input layer, processes them via one or more hidden layers, and finally produces outputs through the output layer [30], as shown in Figure 2(a). RBF is a three-layer feedforward neural network, as illustrated in Figure 2(b). By determining the centers ci and adjusting the connection weights ωij , the network minimizes the discrepancy between its outputs and the target values [31]. In this study, BP and RBF networks serve as reference surrogate models to benchmark performance against SVR.

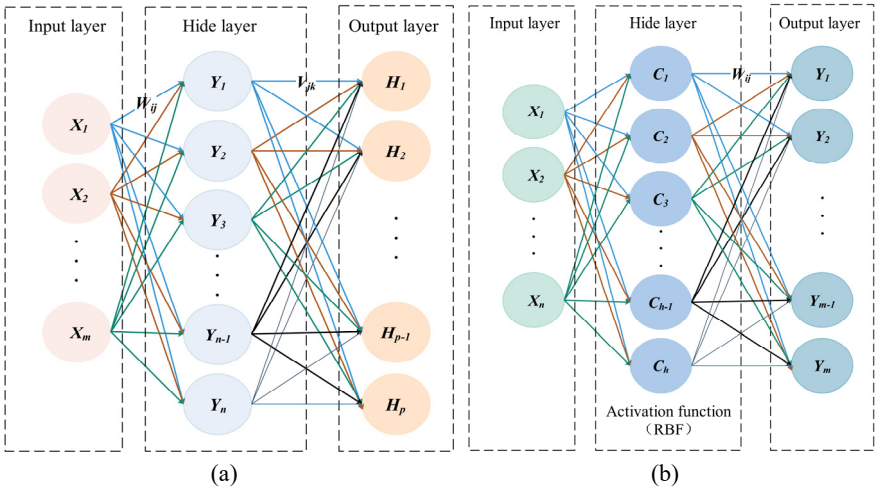

Figure 2. This figure shows the topology of the two models, which consists of input layer, hidden layer and output layer. (a) BP neural network topology diagram; (b) RBF neural network topology diagram.

2.3.2 Support Vector Regression (SVR)

SVR originates from Support Vector Machines (SVM) in statistical learning theory. As illustrated in Figure 3. SVR is particularly effective for regression problems involving high-dimensional data or relatively small sample sizes, offering excellent predictive performance and robustness [32]. In this study, SVR demonstrated the best predictive accuracy among the tested models and was therefore adopted as the primary surrogate model for subsequent analysis. The core optimization problem can be formulated as:

$$min\frac{1}{2}\|\omega\|^2 + C\sum_{i=1}^{N}(\xi_i + \xi_i^*) \tag{5}$$

In the formula: C is the regularization constant, and ξ_i and ξ_i^* are slack variables.

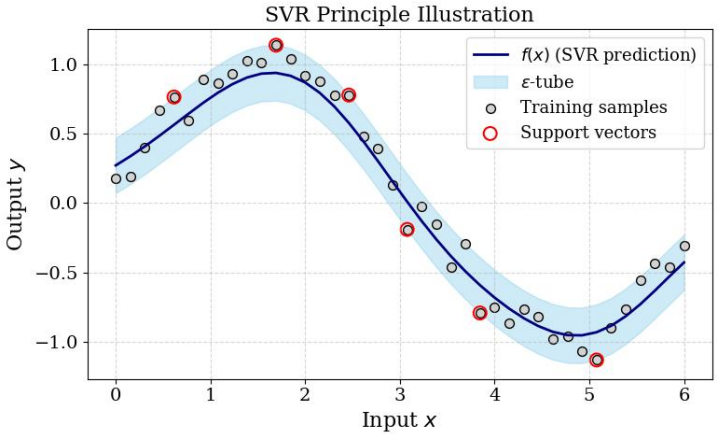

Figure 3. Principle of SVR algorithm

2.3.3 Sparrow Search Algorithm

The Sparrow Search Algorithm (SSA) is a novel swarm intelligence optimization algorithm inspired by the foraging behavior and role differentiation of sparrows. SSA features a simple structure and ease of implementation, and it has demonstrated outstanding performance and fast convergence in various fields such as continuous function optimization, feature selection, and neural network training [33]. SSA has proven effective in solving many classical optimization problems, particularly those involving large search spaces and complex nonlinear objective functions. Owing to its flexible search mechanism and excellent global search capability, SSA has been widely applied in engineering design optimization, path planning, and parameter tuning tasks [34]. In this study, SSA is applied to optimize the hyperparameters of machine learning models, thereby improving their predictive performance.

3. Materials and Methods

3.1 Parametric Modeling Methods

3.1.1 RDT Basic Parameters

In the process of propeller design optimization, parametric modeling plays a pivotal role in bridging the geometric model with the optimization algorithm. By parameterizing the key structural features of the propeller, flexible control over design variables and automated model generation can be achieved, thereby laying a solid data foundation for subsequent high-throughput simulations and machine learning-based modeling. In this study, the RDT is selected as the research object, the principal design parameters selected for analysis include: pitch ratio (PR), disk ratio (DR/A_oA_e), blade number (Z), propeller tip diameter (D).

3.1.2 RDT 3D Modeling

In this study, the Ka4-70 series ducted propeller is adopted as the baseline model for design and analysis. A reverse thickness design approach is applied to adjust the blade thickness distribution, aiming to balance structural strength and hydrodynamic performance, as illustrated in the figure 4. In (a), *r* represents the sectional radius at a specific point along the blade, and *R* denotes the blade radius. (b) shows the planform view of the Ka4-70 blade. Due to the requirement for a smooth propeller surface and the relatively large curvature at each radial section, direct 3D modeling in CAD software is challenging. Therefore, it is necessary to convert the tabulated profile data into 3D spatial coordinates. Multiple sets of spatial points derived from the blade geometry are then imported into the 3D modeling software for surface reconstruction.By referencing the blade profile table, the 2D profile coordinates of each blade section are obtained. Through a transformation based on basic projection principles, these 2D points are converted into 3D spatial coordinates required for 3D model construction. The projection relationship is illustrated in (c), and the final expression for the 3D coordinate transformation is obtained:

$$\begin{bmatrix} X \\ Y \\ Z \end{bmatrix} = \begin{bmatrix} Y_1 cos\phi - X_1 sin\phi + Lsin\phi \\ rcos(X_1 cos\phi + Y_1 sin\phi - Lcos\phi) \\ -rsin(X_1 cos\phi + Y_1 sin\phi - Lcos\phi) \end{bmatrix}, \phi = \arctan\left(\frac{P}{2\pi r}\right) \tag{6}$$

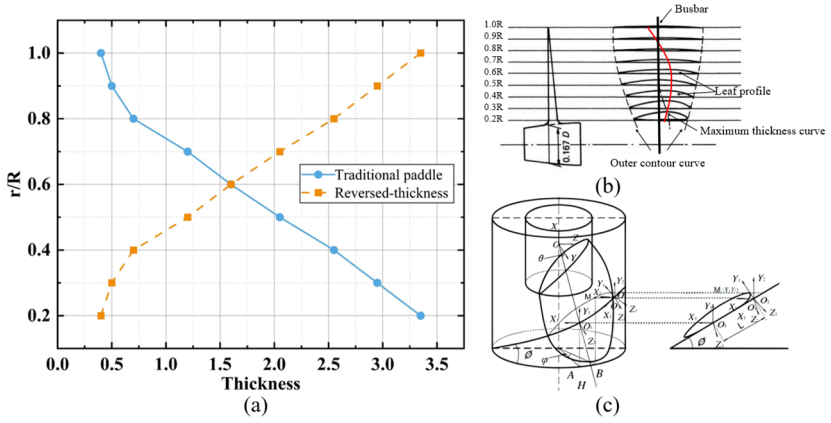

Figure 4. Blade thickness distribution and blade projection diagram

The 3D coordinate points are imported into SolidWorks for further processing. Sectional blade profiles are reconstructed based on these coordinates, and individual sections are lofted and stitched together to generate a complete blade surface. Subsequently, array operations and Boolean unions are applied to replicate and assemble the full propeller model. The overall modeling process is illustrated in the figure 5.

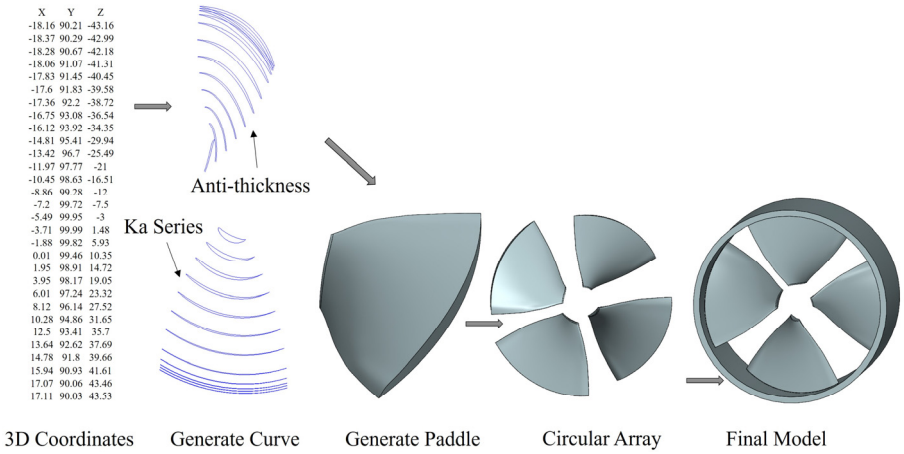

Figure 5. RDT model construction operation flow chart

3.2 Simulation Design

To further improve the fidelity of the numerical simulation, prism layers are generated along all blade surfaces to accurately resolve the near-wall boundary layer characteristics and to ensure that the wall-normal spacing meets the turbulence model requirements. The fluid domain is constructed as a cylindrical control volume with a total axial length of 9D and a diameter of 4D, where *D* denotes the propeller tip diameter. This domain size is selected to minimize the influence of inlet and outlet boundary conditions on the propeller-induced flow field and to allow for fully developed wake formation. Table 1 summarizes the key CFD simulation parameters used in this study.

A velocity inlet is applied at the upstream boundary, and a pressure outlet is assigned downstream. The cylindrical region enclosing the rotor is specified as the rotating reference frame (rotating zone), whereas the remainder of the domain is treated as stationary. This configuration enables accurate capture of the relative motion between the rotating blades and the surrounding fluid. The cross-sectional representation of the computational domain and the mesh structure of the RDT are presented in Figure 6(a) and 6(b), respectively.

During the iterative solution process, the Residuals panel in STAR-CCM+ is utilized to monitor convergence performance. The residual histories, illustrating the stabilization and convergence of the governing equations, are shown in Figure 6(c). Convergence is deemed satisfactory once all residuals drop below the prescribed thresholds and key flow quantities (thrust, torque) exhibit asymptotic behavior.

The simulation incorporates several physical models to ensure robust and realistic flow prediction, including three-dimensional, steady-state, incompressible liquid flow, separated-flow modeling, constant-density formulation, gradient-based reconstruction, and Reynolds-Averaged Navier–Stokes (RANS) turbulence modeling. In particular, the realizable k–ε model with two-layer all-y+ treatment is selected due to its balanced performance in terms of stability, computational efficiency, and capability to handle swirling flows and adverse pressure gradients. The accurate near-wall distance computation further improves the model's ability to resolve the complex boundary layer behavior along the blade surfaces.

As this study involves evaluating a large number of RDT geometric variations, manually repeating the procedures of domain setup, meshing, region assignment, solver configuration, and monitoring becomes highly repetitive and labor-intensive. To overcome this limitation, an automated workflow is established in STAR-CCM+ using macro scripting and external batch-processing tools. This automation framework enables consistent mesh generation, uniform solver settings, and fully reproducible simulation processes across all configurations. The batch script used for automated execution of multiple cases is presented in Figure 6(d).

After the above meshing procedures, the grid quality in the core flow regions was maintained at approximately 0.75, indicating good mesh quality. The total number of cells for the main components was about 1.06 million, which satisfies the accuracy requirements for rim-driven thruster simulations.

To further examine the influence of mesh resolution on the numerical results, simulations were conducted using several grid models with different mesh densities. The results show that when the total number of cells is less than 1.6 million, the predicted propulsion performance exhibits noticeable variations. As shown in Table 2, the relative errors for K_T and K_Q using the 3.6 million mesh are -3.29% and 1.24%, respectively. While the 4.0 million mesh offers slightly higher accuracy, the 3.6 million mesh already provides a satisfactory balance between computational precision and efficiency. Considering that the surrogate model optimization requires a large number of CFD samples, the 3.6 million mesh was selected as the baseline grid to ensure a manageable total computational time while maintaining a high level of fidelity (errors < 5%).

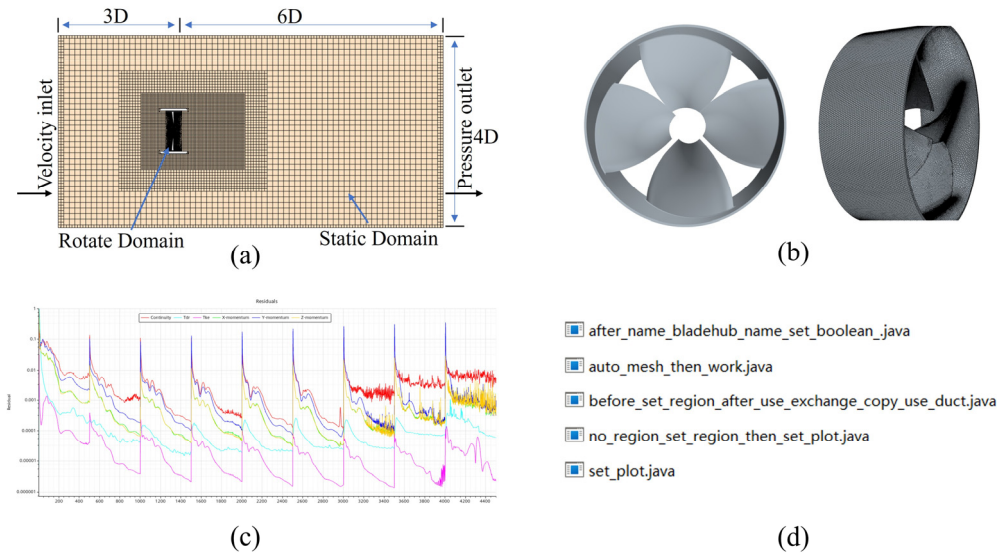

Figure 6. Model meshing and Residuals. (a) shows the division of the domain. (b) shows the division of Blade. (c) shows the residual. (d) list the script files.

Table 1. Summary of Key CFD Simulation Parameters

Category	Parameter	Description / Value
Domain Geometry	Domain Shape / Size	Cylindrical 9D(Length) ×4D (Diameter)
Physics Model	Flow Regime	3D, Steady-state, Liquid (Water), Incompressible, RANS
Turbulence Model	Model Type	Realizable k–ε model
Wall Treatment	Near-wall Handling	Two-layer all-y+ treatment（y+=*40*）
Boundary	Inlet / Outlet	Velocity Inlet / Pressure Outlet
Moving Zone	Motion Type	Rotating Reference Frame (RRF)
Convergence	Residual Threshold	1×10^{-4}(Momentum),1×10^{-5}(Continuity)

Table 2. Thrust and torque coefficients of the RDT with different mesh numbers (PD=1.3, AA=1.1, J=0.3)

Number (million)	KT		Error (%)	10KQ		Error (%)
	CFD	Reference		CFD	Reference	
1.6	0.1564	0.17	-8.00%	0.3149	0.34	-7.38%
2.6	0.1628	0.17	-4.24%	0.3508	0.34	3.18%
3.6	0.1756	0.17	3.29%	0.3442	0.34	1.24%
4.0	0.1732	0.17	1.88%	0.3375	0.34	-0.74%

3.3 Dataset construction

The training dataset used for the neural network model in this study is derived from CFD simulation results, as described in Chapter 3.2. The specific training data are summarized in Table 3. The ranges of the design parameters are as follows: disk ratio from 0.6 to 1.1, pitch ratio from 0.6 to 1.3, and advance ratio from 0.1 to 0.9. In total, 48 models were constructed and analyzed across 9 distinct operating conditions. During the data filtering stage, non-convergent or numerically unstable simulation results were eliminated to ensure the accuracy and stability of the dataset. A total of 345 reliable data samples were retained, each containing three key performance indicators: thrust coefficient, torque coefficient, and propulsive efficiency. These parameters comprehensively describe the nonlinear mapping between the propeller design variables and its hydrodynamic performance. The resulting dataset provides a solid foundation for constructing the subsequent machine learning–based surrogate model.

Table 3. Simulation Dataset

Number	PR	AA	J	Thrust(N)	Torque (N·m)
1	1.3	1	0.1	30.33278681	0.505019301
2	1.2	1.1	0.2	23.72698563	0.404074199
3	1.1	0.9	0.3	18.12534887	0.33528872
…	…	…	…	…	…
345	0.6	0.6	0.1	10.35284163	0.193263492

3.4 Improved Adaptive Sparrow Search Algorithm (IASSA)

The Sparrow Search Algorithm (SSA) is prone to getting trapped in local optima and exhibits high randomness [32]. To address these issues, this paper proposes an Improved Adaptive Sparrow Search Algorithm (IASSA), which reduces the likelihood of premature convergence and demonstrates superior optimization capabilities compared to other algorithms. Firstly, a tent map based on random variables is employed to initialize the population, resulting in a more uniform distribution of individuals, an expanded search space, and enhanced population diversity. During the discoverer phase, an adaptive weight strategy is combined with the Lévy flight mechanism to enable a more comprehensive and flexible search process.

To enhance the algorithm's controllability and produce a more orderly population initialization, a tent map strategy is introduced. The corresponding formula is as follows:

$$z_{i+1} = \begin{cases} 2z_i + rand(0,1) \times \frac{1}{N}, 0 < x_k < \varphi \\ 2(1 - z_i) + rand(0,1) \times \frac{1}{N}, \varphi < x_k < 1 \end{cases} \tag{7}$$

The expression after applying the Bernoulli transformation is given as follows:

$$z_{i+1} = (2z_i) mod 1 + rand(0,1) \times \frac{1}{N} \tag{8}$$

In the formula: N represents the number of particles in the chaotic sequence.

Introducing an adaptive weight can enhance the quality of the discoverers' positions, enabling other individuals to converge more rapidly toward the optimal solution and accelerating the overall convergence speed. The formula for the adaptive weight is given as shown in Equation (9). The improved position update formula for the discoverers is given as shown in Equation (10). By introducing adaptive weights to dynamically adjust the positions of sparrows, the algorithm enhances its search flexibility through different guiding patterns at different stages of the discoverers.

$$w(t) = 0.25 \cos\left(\frac{\pi}{2} \cdot \left(1 - \frac{t}{iter_{max}}\right)\right) \tag{9}$$

$$x_{i,j}^{t+1} = \begin{cases} w(t) \cdot x_{i,j}^{t} \cdot \exp\left(\frac{-i}{\alpha \cdot iter_{max}}\right), R < ST \\ w(t) \cdot x_{i,j}^{t} + Q \cdot L, R \geq ST \end{cases} \tag{10}$$

3.5 Surrogate Model Training

This study established the overall CFD–ML surrogate–IASSA optimization process. Figure 7 shows the three stages of surrogate model training in detail: (i) CFD simulations, performed under various operating conditions to evaluate thrust, torque, and efficiency to generate a performance dataset; (ii) surrogate model construction, training a machine learning algorithm based on the CFD dataset to establish an accurate mapping between design parameters and propulsion performance; and (iii) hyperparameter optimization using IASSA to enhance the predictive power of the surrogate model and ensure robust generalization. The dataset was divided using a five-fold cross-validation method, ensuring that all samples were fully utilized during both training and validation, thereby enhancing the model's robustness and generalization capability.

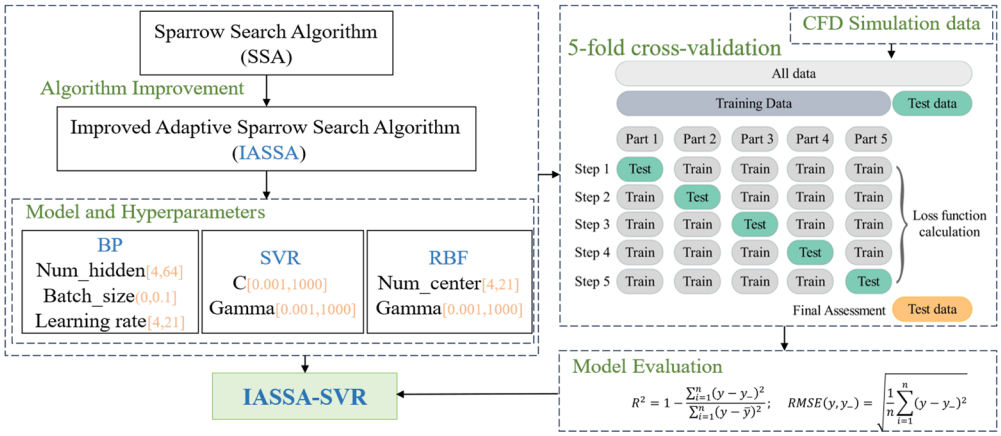

Figure 7. Performance of IASSA on different test functions

4. Results and Discussion

4.1 Validation of Optimization and Surrogate Modeling Tools

4.1.1 Algorithm Performance Test

The proposed IASSA introduces multiple improvements over the standard SSA, enhancing its performance. First, a nonlinear chaotic sequence is used to initialize the population, enhancing the distribution uniformity and global exploration capability. Second, a dynamic weighting factor is incorporated to adaptively balance exploration and exploitation during iterations. These improvements significantly accelerate convergence speed and enhance optimization robustness. The effectiveness of the improved algorithm IASSA is verified by 4 standard test functions. To test the optimization capability of the improved algorithm, 4 standard test functions are selected to verify the performance. The test functions are listed in Table 4.

As shown in Figure 8(a-d), IASSA demonstrates significant improvements in both convergence speed and accuracy. In 4 sets of benchmark function tests, the IASSA curve decreases more rapidly than those of SSA and ISSA [34], reaching a lower final value with smaller fluctuations. This demonstrates significant improvements in both convergence speed and optimization accuracy, as well as enhanced stability performance.

Table 4. Test function table

Test Function
$F_1(x) = \sum_{i=1}^{n} x_i^2$
$F_2(x) = \sum_{i=1}^{n} i x_i^4 + random[0,1)$
$F_3(x) = \sum_{i=1}^{d/4} [(x_{4i-3} + 10x_{4i-2})^2 + 5(x_{4i-1} - x_{4i})^2 + (x_{4i-2} - 2x_{4i-1})^4 + 10(x_{4i-3} - x_{4i})^4]$
$F_4(x) = \sum_{i=1}^{n} x_i^2 + (\sum_{i=1}^{n} 0.5ix)^2 + (\sum_{i=1}^{n} 0.5ix)^4$

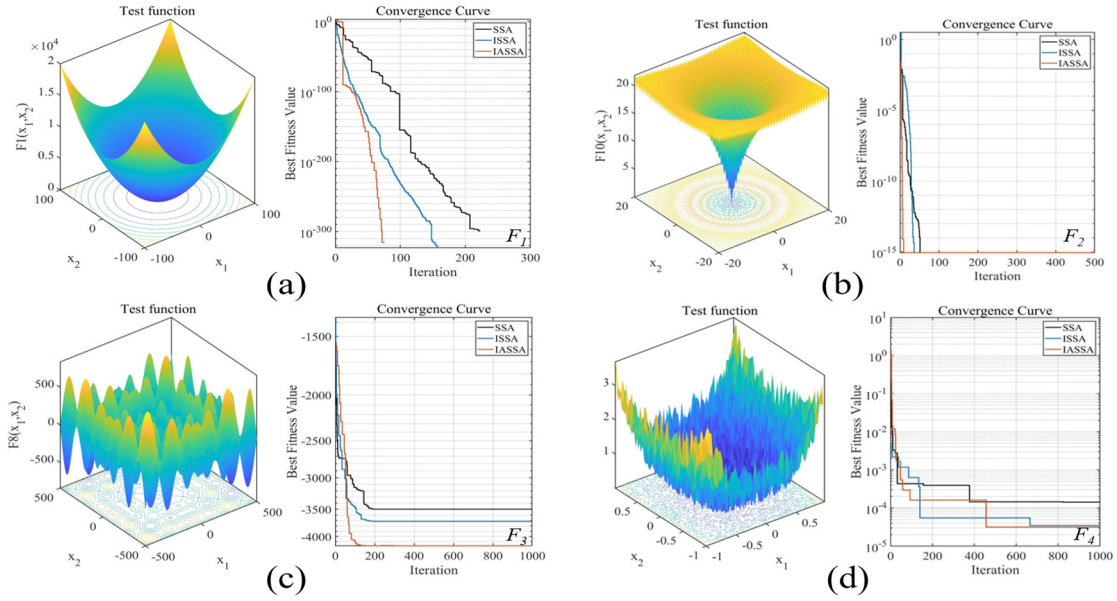

Figure 8. Performance of IASSA on different test functions

4.1.2 Hyperparameter Optimization and Model Evaluation

Hyperparameters strongly influence the predictive capability of machine learning models and differ across algorithms. In this study, the Improved Adaptive Sparrow Search Algorithm (IASSA) was employed to optimize the hyperparameters of BP, RBF, and SVR models. Model performance was assessed using a five-fold cross-validation strategy, which enables each data subset to serve as both training and validation, thereby maximizing data utilization and mitigating overfitting risks in small datasets. This combination of cross-validation and loss-based evaluation ensures a reliable and unbiased assessment of model performance.

Model accuracy was evaluated using the root mean square error (RMSE) and the coefficient of determination (R^2). A lower RMSE reflects higher predictive precision, whereas an R^2 value approaching unity indicates that the model effectively captures the variance of the target variable. Figures 9(a–c) present the fitting results of IASSA-BP, IASSA-RBF, and IASSA-SVR models for both training and testing datasets. In each figure, blue circles denote CFD-derived reference values, and the red line represents model predictions. The IASSA-SVR model demonstrated the best performance, achieving the lowest RMSE and the highest R^2, and was therefore selected as the surrogate model for subsequent optimization.

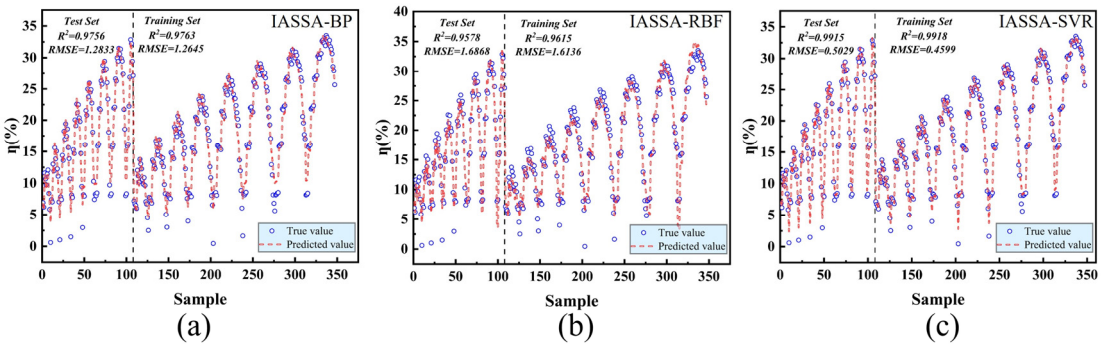

Figure 9. The model fitting results plots of the three models

4.2 Hydrodynamic Performance Analysis of the Design Space

4.2.1 Analysis of RDT simulation results

Figure 10(a) presents the geometric model of the four-blade RDT used for numerical validation and performance analysis. The simulation was conducted at a fixed disk ratio (AA) of 0.7, a pitch ratio (PR) of 1.0, and an advance coefficient (J) of 0.5.

As shown in Figures 10(b) and 10(c), a distinct pressure gradient is observed between the pressure and suction surfaces, which is the fundamental source of propulsive thrust. On the pressure side, high-pressure regions are concentrated near the leading edge (LE). This is attributed to the stagnation effect where the incoming flow directly impinges on the blade surface, converting kinetic energy into static pressure. Conversely, the suction side exhibits a significant low-pressure area, particularly near the blade root and the trailing edge. This pressure drop indicates the acceleration of the fluid over the blade profile, contributing to the majority of the lift-induced thrust in accordance with Bernoulli's principle.

Figure 10(d) illustrates the pressure coefficient (Cp) distribution across a representative cross-section. The maximum Cp values appear at the inlet wall (leading edge), representing the high-load region of the blade. It is noteworthy that for a hubless RDT, the absence of a central hub leads to a unique pressure distribution near the center. The negative pressure zones observed near the blade root suggest a high localized flow velocity, which requires careful design to avoid the risk of cavitation under high-load conditions. The clear distinction between the high-pressure zone on the face and the low-pressure zone on the back confirms that the current RDT design effectively establishes the necessary pressure difference to generate the required axial thrust at J=0.5.

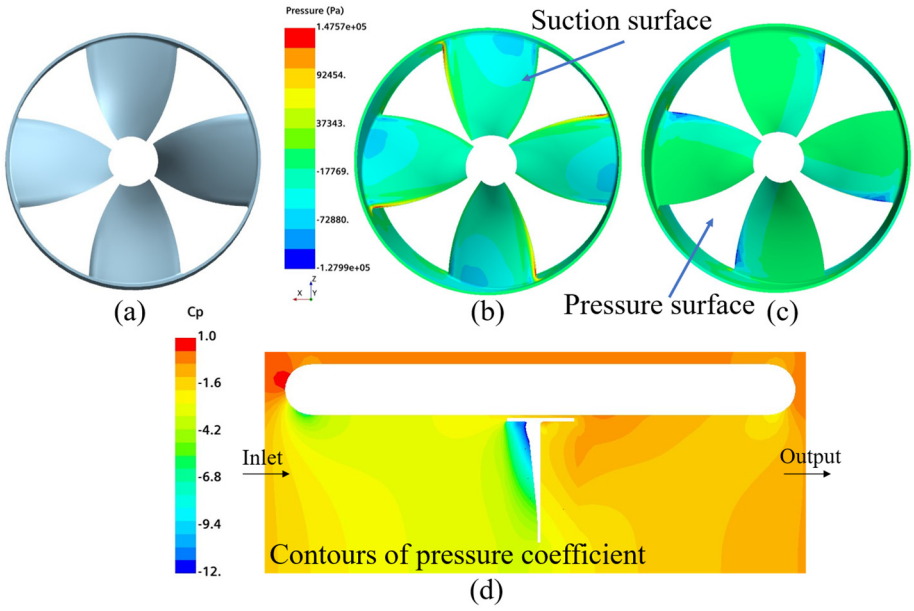

Figure 10. Pressure coefficient contour map

4.2.2 Analysis of the simulation data

Based on initial CFD simulation data (345 samples), the figure 11 illustrates the overall trends of the thrust coefficient, torque coefficient, and propulsive efficiency with respect to pitch ratio, disk ratio, and advance coefficient. The results show that, as the advance coefficient increases, both the thrust and torque coefficients decrease, while the propulsive efficiency initially rises and then declines, indicating a distinct optimal operating range. Variations in pitch ratio and disk ratio exert significant and coupled effects on performance, with different parameter combinations leading to substantial differences in efficiency under various operating conditions. These findings reveal the complex nonlinear interactions among the RDT design parameters, indicating that the optimization problem is not only multivariate but also highly non-convex. Reliance on empirical methods or univariate analyses is unlikely to achieve globally optimal designs. Therefore, it is necessary to employ machine learning surrogate models to enable efficient exploration of the high-dimensional design space, thereby significantly enhancing both the overall performance and design efficiency of the propeller.

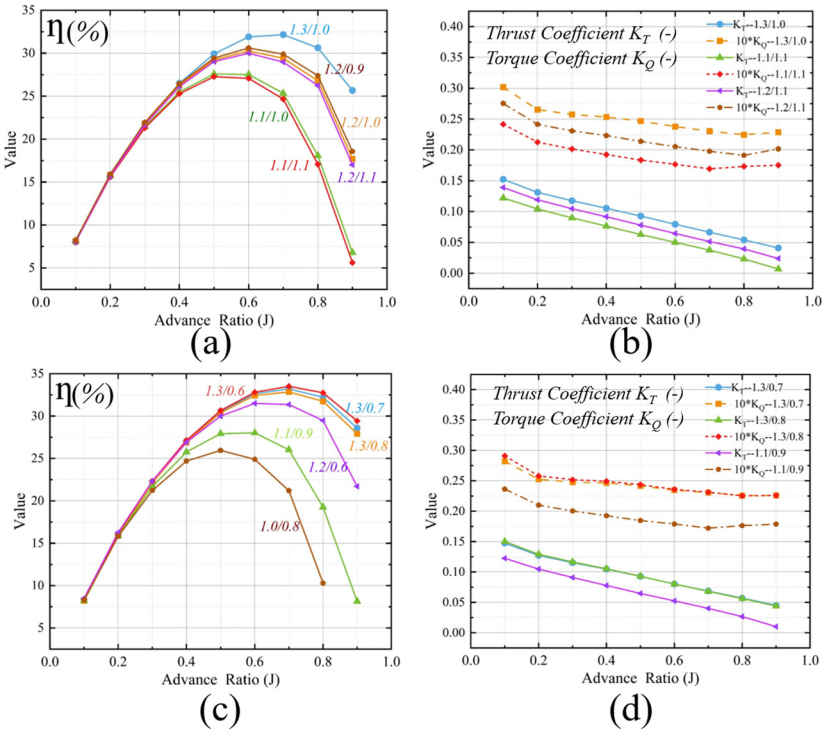

Figure 11. Simulation results RDT hydrodynamic performance comparison chart. (a) and (c) show the relationship between propulsion efficiency and advance coefficient under different parameter combinations. (b) and (d) correspond to the thrust coefficient and torque coefficient under different combinations, respectively.

4.2.3 Analysis of the impact of design variables on performance

Based on the IASSA-SVR model described in Section 3.5, an analysis was conducted by selecting different pitch ratios to determine the corresponding optimal disc area ratios and advance coefficients. This aimed to investigate the effects of disc area ratio and advance coefficient on propulsion efficiency under varying pitch ratio conditions. Considering that RDT propulsion efficiency is significantly reduced when the advance coefficient exceeds 1.1, and that an excessively large disc area ratio may lead to increased viscous friction losses and structural issues such as added weight and potential strength and stiffness problems, predicted data with a disc area ratio greater than 1.1 were excluded. The remaining prediction results were visualized as a contour plot, as shown in Figure 12.

Figure 12 illustrates the effects of disk ratio and advance coefficient on the propulsive efficiency of RDT blades at pitch ratios of 1.0, 1.1, 1.2, and 1.3. In each subfigure, the horizontal axis represents the disk ratio, and the vertical axis denotes the advance coefficient. As shown in Figure 12(a), when the pitch ratio is fixed, the propulsive efficiency increases with the advance coefficient from 0.1 to the range of 0.4-0.7, reaching a peak, and then decreases as the advance coefficient continues to rise. A similar trend is observed with the disk ratio: as it increases from 0.6 to 1.1, the efficiency first improves and then declines. The other subfigures exhibit comparable trends and are not discussed in detail.

Figure 13 presents the influence of pitch ratio and advance coefficient on propulsive efficiency under fixed disk ratios of 0.1, 0.4, 0.6, and 0.8. As the disk ratio increases from 0.6 to 1.3, the propulsive efficiency generally improves. However, with increasing advance coefficient, the efficiency reaches a maximum and then gradually decreases. Figure 14 shows the relationship between pitch ratio, disk ratio, and propulsive efficiency under fixed advance coefficients of 0.1, 0.4, 0.6, and 0.9. When both the pitch ratio and disk ratio are relatively small, the propulsive efficiency remains low. As the pitch ratio increases, a noticeable improvement in efficiency is observed.

The analysis of these contour plots suggests that propulsor design should adopt a system-level, multi-variable optimization strategy. Adjusting a single design parameter in isolation does not guarantee performance improvement. Instead, a coordinated adjustment of pitch ratio and advance coefficient is essential to achieve optimal propulsive efficiency.

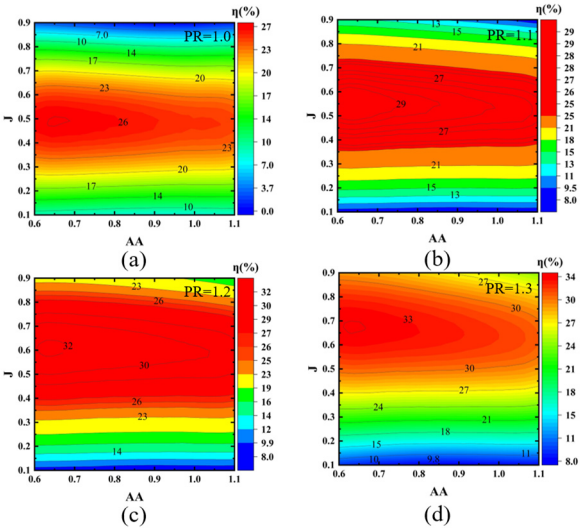

Figure 12. Propulsion efficiency contour map (Fixed Pitch Ratio: the horizontal axis represents the expanded area ratio, and the vertical axis represents the advance coefficient J)

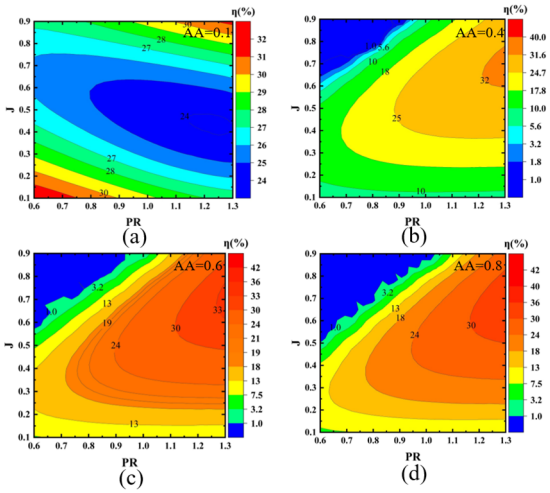

Figure 13. Propulsion efficiency contour map (Fixed Disk Ratio: the horizontal axis represents the pitch ratio (PR), and the vertical axis represents the advance coefficient J)

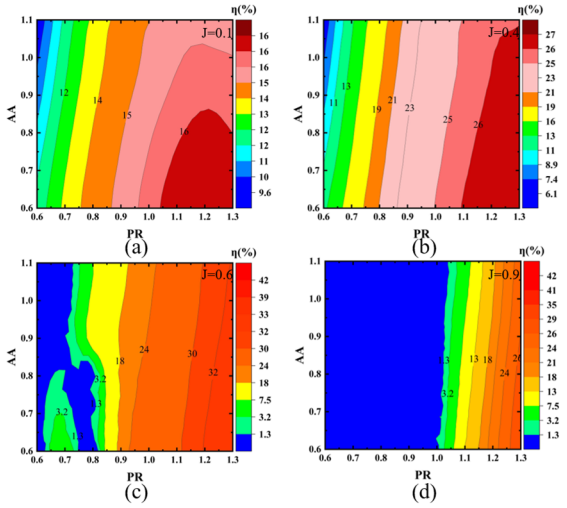

Figure 14. Propulsion efficiency contour map (Fixed Advance Coefficient: the horizontal axis represents the pitch ratio, and the vertical axis represents the expanded area ratio)

4.3 Optimization Results and Analysis

In this study, the SVR model establishes an accurate mapping between the design parameters of the RDT blade and its propulsion efficiency. The improved adaptive sparrow search algorithm (IASSA) is then employed to explore this mapping space efficiently and identify the optimal combination of design parameters. The optimization objective is to maximize the propulsion efficiency (η), which is a key performance indicator of hydrodynamic performance. Therefore, the optimization problem can be formulated as follows:

$$\begin{cases} \max\limits_{x} \eta = f(x_1, x_2, x_3), \eta > 0 \\ x_1 \in [0.6,1.1] \\ x_2 \in [0.6,1.3] \\ x_3 \in [0.1,0.9] \end{cases} \tag{11}$$

After iterative optimization, the optimal parameter configurations under different advance coefficients were obtained, as summarized in Table 5. Due to issues such as engineering implementation, the final value is rounded to two decimal places. Since the advance coefficient is related to the flow velocity, the advance coefficient is fixed, and the optimal combination of the disk ratio and pitch ratio is sought within an appropriate range. The results of Simulation comparative analysis show that the propulsion efficiency is improved under the optimal parameter combination, with the propulsion efficiency increased by 3-7%. Of course, it is also possible to fix the disk ratio or pitch ratio and find the best combination of the other two sets of parameters. The experimental method is the same as the above, so this part will not go into details here. Table 6 and Table 7 are provided for reference. Based on the surrogate models developed in this study, the optimal combination of design parameters can be determined within their respective ranges, thereby significantly improving propulsive efficiency under various operating conditions.

Table 5. Optimal parameter configuration under fixed advance coefficient

Pitch Ratio	Disk Ratio	Advance Coefficient	Efficiency	Reference value
1.09	0.68	0.1	8.6605	8.3219
1.30	0.68	0.2	16.1129	15.0461
1.30	0.67	0.3	22.2628	21.2382
1.30	0.64	0.4	27.1495	26.1324
1.29	0.62	0.5	30.7730	29.6618
1.22	0.60	0.6	33.0613	31.4941
1.16	0.60	0.7	33.5461	32.3585
1.30	0.60	0.8	32.9809	31.7448
1.30	0.61	0.9	30.2512	29.4279

Table 6. Optimal parameter configuration under fixed pitch ratio

Pitch Ratio	Disk Ratio	Advance Coefficient	Efficiency	Reference value
0.6	0.61	0.31	13.87429433	13.75191
0.7	0.60	0.36	17.31038538	16.87537
0.8	0.62	0.41	20.76490547	20.66123
0.9	0.60	0.47	24.07379126	23.81467
1.0	0.60	0.52	27.07321707	26.83266
1.1	0.61	0.58	29.60996557	29.43925
1.2	0.60	0.64	31.74142857	31.35849
1.3	0.61	0.70	33.60841261	33.50782

Table 7. Optimal parameter configuration under fixed disk ratio

Pitch Ratio	Disk Ratio	Advance Coefficient	Efficiency	Reference value
1.30	0.6	0.69673996	33.60910047	33.50782
1.29	0.7	0.70060883	33.17249575	33.20835
1.29	0.8	0.694799805	33.16697413	32.85095
1.30	0.9	0.68378906	32.75367141	32.53940
1.28	1.0	0.67412109	32.37536188	32.15583

4.4 Optimization results display and performance comparison

After determining the optimal parameter combination, the corresponding thrust and torque were calculated through CFD simulations to obtain the propulsive efficiency under this configuration. Table 8 compares the differences in propulsive efficiency between the optimal parameter combination and the pre-optimization reference values at various advance coefficients. Figure 15 further illustrates the variation trends of propulsive efficiency with different advance coefficients, including the predictions from the surrogate model developed in this study, the CFD results corresponding to the optimal combination, and the reference values from the baseline model. The three curves exhibit consistent trends, and compared with the baseline model, the propulsive efficiency is improved by approximately 3-7%. In addition, the variations in thrust and torque coefficients are consistent with theoretical expectations, further validating the accuracy and reliability of the optimization results.

Table 8. Optimal parameter configuration under fixed disk ratio

PR	AA	J	Thrust(N)	Torque (N·m)	Model value	CFD value	Reference
1.09	0.68	0.1	24.50856935	0.377476925	8.6605	8.680144793	8.3219
1.30	0.68	0.2	25.92007144	0.430203216	16.1129	16.10986701	15.0461
1.30	0.67	0.3	23.01473047	0.41046058	22.2628	22.48822155	21.2382
1.30	0.64	0.4	20.46819884	0.398274195	27.1495	27.48253997	26.1324
1.29	0.62	0.5	17.98474571	0.388110716	30.7730	30.9754832	29.6618
1.22	0.60	0.6	14.19912207	0.354107249	33.0613	32.16453989	31.4941
1.16	0.60	0.7	13.43689268	0.378644389	33.5461	33.20968683	32.3585
1.30	0.60	0.8	11.59945687	0.382810750	32.9809	32.40730635	31.7448
1.30	0.61	0.9	9.316653084	0.377440909	30.2512	29.69975608	29.4279

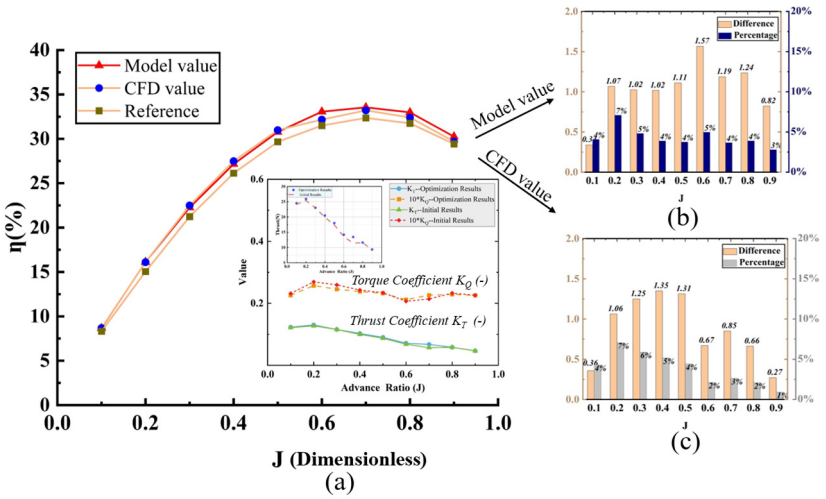

Figure 15. Comparison of propulsion efficiency. (a) The CFD simulation results and model prediction results under the new combination. (b) Percentage difference between model predictions and reference values. (c) Percentage of difference between CFD simulation value and reference value

5. Conclusions

This study successfully addressed the complex, multi-variable, and nonlinear problem of hydrodynamic performance optimization for hubless Rim-Driven Thruster (RDT) blades. The principal contribution of this work lies in the development and validation of a robust, data-driven optimization framework that integrates high-fidelity CFD simulations, a machine-learning-based surrogate model, and a novel Improved Adaptive Sparrow Search Algorithm (IASSA). This integrated approach effectively overcomes the limitations of traditional experimental trial-and-error methods and computationally expensive direct CFD-based optimization strategies.

The effectiveness of the proposed framework was demonstrated through several key findings. First, the newly developed IASSA exhibited superior optimization capability, achieving faster convergence and higher accuracy than conventional algorithms in benchmark tests. Second, the IASSA-optimized Support Vector Regression (SVR) surrogate model achieved excellent predictive performance ($R^2 > 0.99$), accurately capturing the nonlinear relationship between blade design parameters and hydrodynamic performance. Finally, the application of the validated framework led to optimized blade parameter configurations, resulting in a CFD-verified propulsive efficiency improvement of 3% to 7% compared with the baseline design across a range of operating conditions. Detailed flow analysis indicates that this performance gain is primarily attributed to the reduction of tip-leakage energy losses and a more uniform pressure distribution on the blade surfaces, which suppresses flow separation and enhances energy conversion efficiency.

The significance of this study extends beyond the observed efficiency improvements. The proposed CFD–SVR–IASSA framework provides an efficient and practical alternative to conventional RDT design approaches, enabling faster design iteration, reduced computational cost, and enhanced adaptability to application-specific requirements. This contribution helps bridge the gap between theoretical optimization methodologies and the practical engineering design of high-efficiency, entanglement-resistant hubless thrusters for small marine vehicles.

Despite the promising results, several limitations remain. The present optimization primarily focused on hydrodynamic efficiency, while structural performance was not fully integrated into the optimization loop. Therefore, future research will focus on the development of a comprehensive multi-objective optimization framework that simultaneously considers propulsive efficiency, thrust performance, and structural reliability. In addition, future work will incorporate a wider range of operating conditions and conduct experimental validation of the optimized designs in underwater testing facilities to further confirm real-world performance improvements.

Conflicts of Interest: The authors declare no conflict of interest.

References

[1] X. Yan, X. Liang, W. Ouyang, Z. Liu, B. Liu, and J. Lan, “A review of progress and applications of ship shaft-less rim-driven thrusters,” Ocean engineering, vol. 144, pp. 142-156, 2017, doi: https://doi.org/10.1016/j.oceaneng.2017.08.045.

[2] Industrial Technology Research Institute of Huazhong Industrial Technology Research Institute of Huazhong University of Science and Technology, Guangdong, A high-efficiency shaftless rim propeller, Chinese Patent CN202210866932.9, Sep. 2, 2022. [Online] Available: https://patents.google.com/patent/CN114987725A

[3] Y. Yang, “High-efficiency ship propeller based on electric direct drive without shaft rim,” In IOP Conference Series: Earth and Environmental Science, IOP Publishing, vol. 651, no. 2, p. 022068, Feb. 2021. [Online] Available: https://iopscience.iop.org/article/10.1088/1755-1315/651/2/022068

[4] Y. Lei, “Parameter analysis and open water test design of lightweight rim thruster,” M.S. thesis, Dept. of Naval Architecture, Harbin Institute of Technology, Harbin, China, 2022, doi: https://doi.org/10.27060/d.cnki.ghbcu.2024.000100.

[5] B. W. Song, Y. J. Wang, and W. L. Tian, “Open water performance comparison between hub-type and hubless rim driven thrusters based on CFD method,” Ocean Engineering, vol. 103, pp. 55-63, 2015, doi: https://doi.org/10.1016/j.oceaneng.2015.04.074.

[6] L. Peng. “Research on performance prediction and optimization of submarine main thruster rim thruster,” M.S. thesis, Dept. of Naval Architecture, Harbin Engineering University, Harbin, China, 2024, doi: https://doi.org/10.27060/d.cnki.ghbcu.2024.000100.

[7] M. S. Kim and S. A. Kim, “Design and experimental verification of hubless rim-driven propulsor consisting of bearingless propeller for an unmanned underwater drone,” Energies, vol. 16, no. 21, 7458, 2023, doi: https://doi.org/10.3390/en16217458.

[8] Y. Chen, "Optimization design of shaftless rim thruster for small unmanned boat," M.S. thesis, Dept. of Naval Architecture, Huazhong University of Science and Technology, Wuhan, China, 2023, doi: https://doi.org/10.27157/d.cnki.ghzku.2023.003163.

[9] Q. M. Cao, W. F. Zhao, D. H. Tang, and F. W. Hong, "Effect of gap flow on the torque for blades in a rim driven thruster without axial pressure gradient. Procedia Engineering," vol. 126, pp. 680-685, 2015, doi: https://doi.org/10.1016/j.proeng.2015.11.265.

[10] Copenhagen Subsea. Product Manual: Rim-Driven Thruster. (2020). [Online] Available: https://magazines.marinelink.com/Magazines/MarineTechnology

[11] Rolls-Royce Marine. Azimuthing Rim-Driven Thruster Brochure. (2018). [Online] Available: https://www.rivieramm.com/news-content-hub/news-content-hub

[12] B. Liu and M. Vanierschot, "Numerical study of the hydrodynamic characteristic's comparison between a ducted propeller and a rim-driven thruster," Applied Sciences, vol. 11, no. 11, 4919, 2021, doi: https://doi.org/10.3390/app11114919.

[13] Y. Shu, W. Daamen, H. Ligteringen, and S. P. Hoogendoorn, "Influence of external conditions and vessel encounters on vessel behavior in ports and waterways using Automatic Identification System data," Ocean Engineering, vol. 131, pp. 1-14, doi: https://doi.org/10.1016/j.oceaneng.2016.12.027.

[14] A. B. Mayfield and A. C. Dempsey, "Environmentally-Driven Variation in the Physiology of a New Caledonian Reef Coral. In Oceans, vol. 3, no. 1, pp. 15-29, Jan. 2022, doi: https://doi.org/10.3390/oceans3010002.

[15] L. Kort, Elektrisch angertriebene schiffsschraube, German Patent, 688(114), 13, 1940. [Online] Available: https://patents.google.com/patent/DE743672C/de

[16] K. J. Anderson, Writing in the Advanced hull form inshore demonstrator model strut and propulsor Performance in uniform flow, Technical Report No. NSWCCD-50-TR-2005/012NSWCCD,16—19. ISBN：9781423510772

[17] Rolls-Royce Delivers First Permanent Magnet Tunnel Thruster, MarineLink, 2012-09-21. [Online] Available: https://www.marinelink.com/news/rollsroyce-permanent347837

[18] N. W. Bulten, "Numerical analysis of flow around a thruster," In Dynamic Positioning Conference. (2006). [Online] Available: https://dynamic-positioning.com/wp-content/uploads/2025/12/thrusters_bulten_pp.pdf

[19] Wärtsilä Corporation, Wärtsilä Ship Power Product Catalogue [R]. 2011. [Online] Available: https://www.scribd.com/

[20] Guangzhou Offshore Engineering, The first domestically produced shaftless rim-type marine electric propulsion system obtains CCS certification. (2023). [Online] Available: https://www.eworldship.com/html/2023/Manufacturer_1129/198464.html

[21] Z. Q. Rao, "Research on optimization design method of submarine propulsion hydrodynamic performance based on panel method," Ph.D. dissertation, Dept. of Naval Architecture and Ocean Engineering, Shanghai Jiao Tong University, Shanghai, China, A Study of Hydrodynamic Optimization Approach of Submarine Propulsors Based on Panel Method - CNKI, 2017.

[22] S. Gaggero, C. M. Rizzo, G. Tani, and M. Viviani, "EFD and CFD design and analysis of a propeller in decelerating duct," International Journal of Rotating Machinery, 2012, doi: https://doi.org/10.1155/2012/823831.

[23] W. Jiang, X. Shen, L. Liu, and T. Bian, "Numerical analysis of the effect of the blade number on the hydrodynamic performance of shaftless rim-driven thruster," Proceedings of the Institution of Mechanical Engineers, Part M: Journal of Engineering for the Maritime Environment, vol. 237, no. 3, pp. 588-596, 2023, doi: https://doi.org/10.1177/14750902221145785.

[24] K. I. M. Hyoung-Ho, "Performance analysis of hubless rim-driven thruster based on the number of blades: a CFD approach," Journal of the Korean Society of Fisheries and Ocean Technology, vol. 60, no. 1, pp. 80-86, 2024, doi: https://doi.org/10.3796/KSFOT.2024.60.1.080.

[25] W. Jiang, J. Zhao, T. Bian, and W. Yu, "Numerical analysis of the effect of the duct geometry on the hydrodynamic performance of rim-driven thruster," Proceedings of the Institution of Mechanical Engineers, Part M: Journal of Engineering for the Maritime Environment, vol. 239, no. 1, pp. 178-191, 2025, doi: https://doi.org/10.1177/14750902241242248.

[26] Y. B. Pyeon and K. I. M. Hyoung-Ho, "A study on optimization of duct shape of electric hubless rim-driven propeller," Journal of the Korean Society of Fisheries and Ocean Technology, vol. 59, no. 1, pp. 65-73, 2023. [Online] Available: https://scholarworks.gnu.ac.kr/handle/sw.gnu/30217

[27] B. Liu, M. Vanierschot, and F. Buysschaert, "Optimization design of the duct of a rim-driven thruster using the adjoint approach," Ocean Engineering, vol. 278, 114293, 2023, doi: https://doi.org/10.1016/j.oceaneng.2023.114293.

[28] L. G. Qiang and W. Ouyabg, "Analysis of hydrodynamic characteristics and influencing factors of shaftless wheel rim thruster," Ship Science and Technology, vol. 45, no. 7, pp. 126-131, 2023, doi: https://doi.org/10.3404/j.issn.1672-7649.2023.07.024.

[29] S. Ke and Y. Bangcheng, "A comparative study on the hydrodynamics and energy loss characteristics between a rim-driven thruster and a ducted propeller," Ship Science and Technology, vol. 45, no. 15, pp. 41-45, 2023, doi: https://doi.org/10.3404/j.issn.1672-7649.2023.15.008.

[30] F. Weiyu, C. Shunhuai, and Z. Long, "Marine propeller optimization method based on neural network," Ship Science and Technology, vol. 45, no. 2, pp. 47-51, 2023, doi: https://doi.org/10.3404/j.issn.1672-7649.2023.02.009.

[31] B. Tao, L. Liangliang, C. Wenhao, J, Wen, and L, Zhiwen, "Multi-objective optimization design of shaftless rim-driven thruster," Proceedings of the Institution of Mechanical Engineers, Part M: Journal of Engineering for the Maritime Environment, vol. 238, no. 3, pp. 633-639, 2024, doi: https://doi.org/10.1177/14750902231188393.

[32] X. Su, X. He, G. Zhang, Y. Chen, and K. Li, "Research on SVR water quality prediction model based on improved sparrow search algorithm," Computational Intelligence and Neuroscience, vol. 2022, no. 1, 7327072, 2022, doi: https://doi.org/10.1155/2022/7327072.

[33] B. Li, J. Mao, S. Yin, L. Fu, and Y. Wang, "Path planning of multi-objective underwater robot based on improved sparrow search algorithm in complex marine environment," Journal of Marine Science and Engineering, vol. 10, no. 11, 1695, 2022, doi: https://doi.org/10.3390/jmse10111695.

[34] Q. Liang, B. Chen, H. Wu, and M. Han, "A Novel Modified Sparrow Search Algorithm Based on Adaptive Weight and Improved Boundary Constraints," 2021 IEEE 6th International Conference on Computer and Communication Systems (ICCCS), Chengdu, China, pp. 104-109, 2021, doi: https://doi.org/10.1109/ICCCS52626.2021.9449311

© 2026 by the authors. Copyrights of all published papers are owned by the IJOC. They also follow the Creative Commons Attribution License (https://creativecommons.org/licenses/by-nc/4.0/) which permits unrestricted non-commercial use, distribution, and reproduction in any medium, provided the original work is properly cited.